

Hybrid Batteries

Tuning Electron Delocalization of Redox-Active Porous Aromatic Framework for Low-Temperature Aqueous Zn–K Hybrid Batteries with Air Self-Chargeability

Junhao Wang, Xupeng Zhang, Zhaoli Liu, Jie Yu, Heng-Guo Wang,* Xing-Long Wu, Fengchao Cui, and Guangshan Zhu*

Abstract: Air self-charging aqueous batteries promise to integrate energy harvesting technology and battery systems, potentially overcoming a heavy reliance on energy and the spatiotemporal environment. However, the exploitation of multifunctional air self-charging battery systems using promising cathode materials and suitable charge carriers remains challenging. Herein, for the first time, we developed low-temperature self-charging aqueous Zn–K hybrid ion batteries (AZKHBs) using a fully conjugated hexaazanonaphthalene (HATN)-based porous aromatic framework as the cathode material, exhibiting redox chemistry using K^+ as charge carriers, and regulating Zn-ion solvation chemistry to guide uniform Zn plating/stripping. The unique AZKHBs exhibit the exceptional electrochemical properties in all-climate conditions. Most importantly, the large potential difference causes the AZKHBs discharged cathode to be oxidized using oxygen, thereby initiating a self-charging process in the absence of an external power source. Impressively, the air self-charging AZKHBs can achieve a maximum voltage of 1.15 V, an impressive discharge capacity (466.3 mAhg^{-1}), and exceptional self-charging performance even at -40°C . Therefore, the development of self-charging AZKHBs offers a solution to the limitations imposed by the absence of a power grid in harsh environments or remote areas.

theoretical capacity, environment-friendliness, and low cost.^[1] However, their application is limited, particularly in remote areas or harsh environments where there is no available electricity to power the recharging process. In this regard, a prospective approach is to fabricate a self-charging system via combining AZIBs with environmental-responsive modules (solar, wind, geothermal, air, etc.).^[2] Among these modules, the air is pervasive with regard for natural conditions, making the chemical energy of O_2 a cost-free and readily-available energy resource, therefore, exploiting self-charging systems using air is a promising candidate for self-powered battery systems.^[3] Unfortunately, these AZIBs still exhibit poor cycle stability and air charging ability. Therefore, developing novel aqueous batteries with chemical self-chargeability is exciting and challenging.

In general, the electrolyte used to define the charge carrier of AZIBs exhibits a significant impact on their electrochemical behavior.^[4] As the most common carrier of AZIBs, Zn^{2+} ions have large hydration radius, which must overcome the higher desolvation barrier during the extraction process, resulting in slow reaction kinetics. Furthermore, the uncontrollable dendrite growth and irreversible byproduct formation of the Zn anode resulted in the unsatisfactory long-term stability and safety hazards.^[5] In contrast, K^+ ions as charge carriers have recently gained attention owing to its low charge/radius ratio and weak hydration structure, which may result in the enhanced reaction kinetics and air-chargeability.^[6] Furthermore, the incorporation of a Zn–K hybrid ion electrolyte (known as aqueous Zn–K hybrid batteries, AZKHBs) can change the coordination environment of the hydrated Zn^{2+} , reduce H_2O molecule activity, thereby enhancing the rechargeability of the Zn anode and mitigating the side reaction caused by the H_2O . Interestingly, the bonds formed by combining K^+ ions are easily broken by O_2 oxidation, resulting in a self-charging mechanism.^[7] Particularly, these redox reactions occur between the host material and O_2 , necessitating the urgent investigation of advanced host materials for creative air self-charging battery systems.

Organic electrode materials are gaining attention owing to their outstanding advantages in terms of environmental friendliness, structural designability and abundant resources.^[8] π -conjugated porous organic polymers (POPs) have been exhibited as prospective electrode materials for AZIBs owing to their large internal space, structural diversity, and high physicochemical stability.^[9] Their π -conjugated structures can be manipulated to achieve electron delocalization, resulting in

Introduction

Aqueous Zn-ion batteries (AZIBs) have been emerging as a novel type of largescale energy storage device due to their high

[*] J. Wang, X. Zhang, Z. Liu, J. Yu, H.-G. Wang, F. Cui, G. Zhu
Key Laboratory of Polyoxometalate and Reticular Material Chemistry
of Ministry of Education and Faculty of Chemistry, Northeast
Normal University, 5268 Renmin Street, Changchun, 130024, P. R.
China
E-mail: wanghg061@nenu.edu.cn
zhugs@nenu.edu.cn

X.-L. Wu
MOE Key Laboratory for UV Light-Emitting Materials and Technol-
ogy and School of Physics, Northeast Normal University, 5268
Renmin Street, Changchun, 130024, P. R. China

increased intrinsic conductivity and high redox kinetics.^[10] Furthermore, the functional design of the structural units enables precise presetting of redox-active centers at the predicted skeleton, resulting in electrode materials with exceptional electrochemical properties.^[11] Notably, their redox chemistry focuses on the rearrangement of chemical bonds, which may be occurred more easily with oxygen present. As previously stated, developing redox-active π -conjugated POPs to construct new-style aqueous batteries using chemical self-chargeability is urgently needed. However, no examples of π -conjugated POPs based on AZKHBs, let alone using chemical self-chargeability, have been reported yet.

We successfully synthesized the fully conjugated hexaazanonaphthalene (HATN)-based porous aromatic framework (PAF-305) and demonstrated its application as an AZKHBs cathode material for the first time, even with chemical self-chargeability over a wide temperature range. PAF-305 exhibits impressive electronic conductivity, high utilization of the redox-active site, and fast redox kinetics owing to super-electron delocalization. AZKHBs exhibit an impressive discharge capacity (209.9 mAh g^{-1} , 50 mA g^{-1}), excellent cycle stabilities (84 % capacity retention with 1600 cycles, 10 Ag^{-1}), outstanding rate performance (76.9 mAh g^{-1} , 10 Ag^{-1}), and a unique work mechanism in which Zn^{2+} ions are plated/stripped at the anode and K^{+} ions are inserted/extracted at the cathode, based on the reversible conversion between $\text{C}\equiv\text{N}$ and $\text{C}-\text{N}-\text{K}$ conversion supported by theoretical and experimental evidence. Interestingly, the presence of O_2 can cause the $\text{N}-\text{K}$ bond of the cathode discharge product to break via redox reaction, allowing chemically self-charging AZKHBs to be constructed, demonstrating improved electrochemical performance. Furthermore, the flexible pouch AZKIBs were assembled to exhibit their application potential.

Results and Discussion

To achieve fully conjugated two-dimensional (2D) redox-active PAFs with super-electronic delocalization, a bottom-up polymerization strategy was used to polymerize rigidly conjugated hexaminohexaazatrinaphthalene (HAHATN) with abundant $\text{C}\equiv\text{N}$ active sites and pyrene-4,5,9,10-tetrone (PTO) that can extend its conjugate system. A 2D redox-active PAF was synthesized from HAHATN and PTO using the Schiff base reaction, yielding a honeycomb-shaped 2D structure (Figures 1a and S1). The synthesized PAF-305 was then analyzed using ^{13}C solid-state NMR and Fourier transform infrared spectroscopy (FT-IR). The disappearance of stretching vibration peaks of $-\text{NH}_3^{+}$ at 3043 and 3142 cm^{-1} , the near disappearance peak of the $\text{C}=\text{O}$ bond at 1681 cm^{-1} , and a dominant peak at 129.1 ppm in the solid state ^{13}C NMR,^[12] confirm the successful synthesis of PAF-305 (Figures S2–S3). Furthermore, PAF-305 is amorphous, as observed via powder X-ray diffraction (Figure S4), and exhibits a surface area of $79.8 \text{ m}^2 \text{ g}^{-1}$ with type II isotherms (Figure S5). The PAF-305 morphology was studied using scanning electron microscopy (SEM) and transmission electron microscopy (Figure S6). PAF-305 exhibits an irregular spherical shape, and the near overlap of the N and C elemental images confirm its

homogeneous chemical composition. Moreover, PAF-305 exhibits good thermal stability (Figure S7). Furthermore, electron delocalization alters electron distribution within the molecule, increasing the intrinsic conductivity and redox kinetics of PAF-305, which exhibits exceptional electrochemical properties. First, the location of the active site of the PAF-305 unit was determined by using density functional theory (DFT) calculations. The electrostatic potentials reveal that the negative charge maxima (grass green region) are distributed within the hexagonal pores of the PAF-305 unit, with six suitable cation-accommodating sites surrounded by strongly electronegative N atoms (Figure 1b). The local orbit locator- π (LOL- π) can analyze PAF-305's stable structure owing to the delocalization of the π -electrons.^[13] Figure 1c illustrates that the π -electrons are homogeneously distributed within the framework of the diquinoxalino [2,3-a:2',3'-c] phenazine (HATN) or quinoxalino[2,3':9,10] phenanthrol [4,5-abc] phenazine (DPP). Even after combining HATN and DPP to form PAF-305, the delocalization orbitals of the π -electron can still be observed. Furthermore, the π -electron delocalized orbital locator demonstrates that π -electrons are primarily distributed in the red region, indicating favorable delocalized paths, consistent with the LOL- π maps (Figure 1d). Furthermore, electron delocalization influences the properties of the highest occupied molecular orbital (HOMO) and the lowest unoccupied molecular orbital (LUMO). PAF-305 unit has a lower band gap of 2.40 eV compared to DPP (3.78 eV) and HATN (3.59 eV), exhibiting higher electronic conductivity (Figure 1e).^[14] Furthermore, the lowest LUMO indicates that the PAF-305 unit exhibits a higher electron affinity and redox potential, implying improved electrochemical performance. Generally, the reduced density gradient and correlated gradient isosurface are typically used to detect weak interactions.^[15] Figures 1f and S8 depict green peaks at -0.02 to 0.00 a.u. of the $(I_2)r$ symbol, indicating a weak π - π interaction within the layers of the PAF-305 unit. This allows for out-of-plane interactions and effective interfacial charge transfer, leading to efficient redox kinetics for PAF-305.

The integration of $\text{Zn}(\text{OTF})_2 + \text{KOTF}$ ($\text{Zn}-\text{K}$) hybrid ion electrolyte provides electrolyte modification and introduces charge carriers. First, the improvement in electrolyte performance caused by the introduction of KOTF was investigated. Molecular dynamics (MD) simulations reveal Zn^{2+} ions solvation structure in different electrolytes (Figures 2a,b).^[16] The radial distribution functions (RDFs) and coordination numbers of Zn^{2+} and H_2O in the electrolyte are shown in Figure 2c. The first solvation shell of Zn^{2+} is in coordination with six H_2O in the $\text{Zn}(\text{OTF})_2$ electrolyte, whereas almost all of the OTF^{-} anions are separated from Zn^{2+} by water, probably owing to the high dielectric constant of water exhibiting a strong ability to separate cation-anion pairs. However, the addition of KOTF results in a completely different solvation structure. Number of H_2O molecules in the first solvation shell of Zn^{2+} decreases, while OTF^{-} dominates. This solvation effect increases the radial association between Zn^{2+} and Zn^{2+} , and the coordination of Zn^{2+} with OTF^{-} , enhancing the kinetic hysteresis and facilitating Zn^{2+} transportation (Figures 2d and S9a). Furthermore, the interactions of different Zn crystalline surfaces with various atoms and

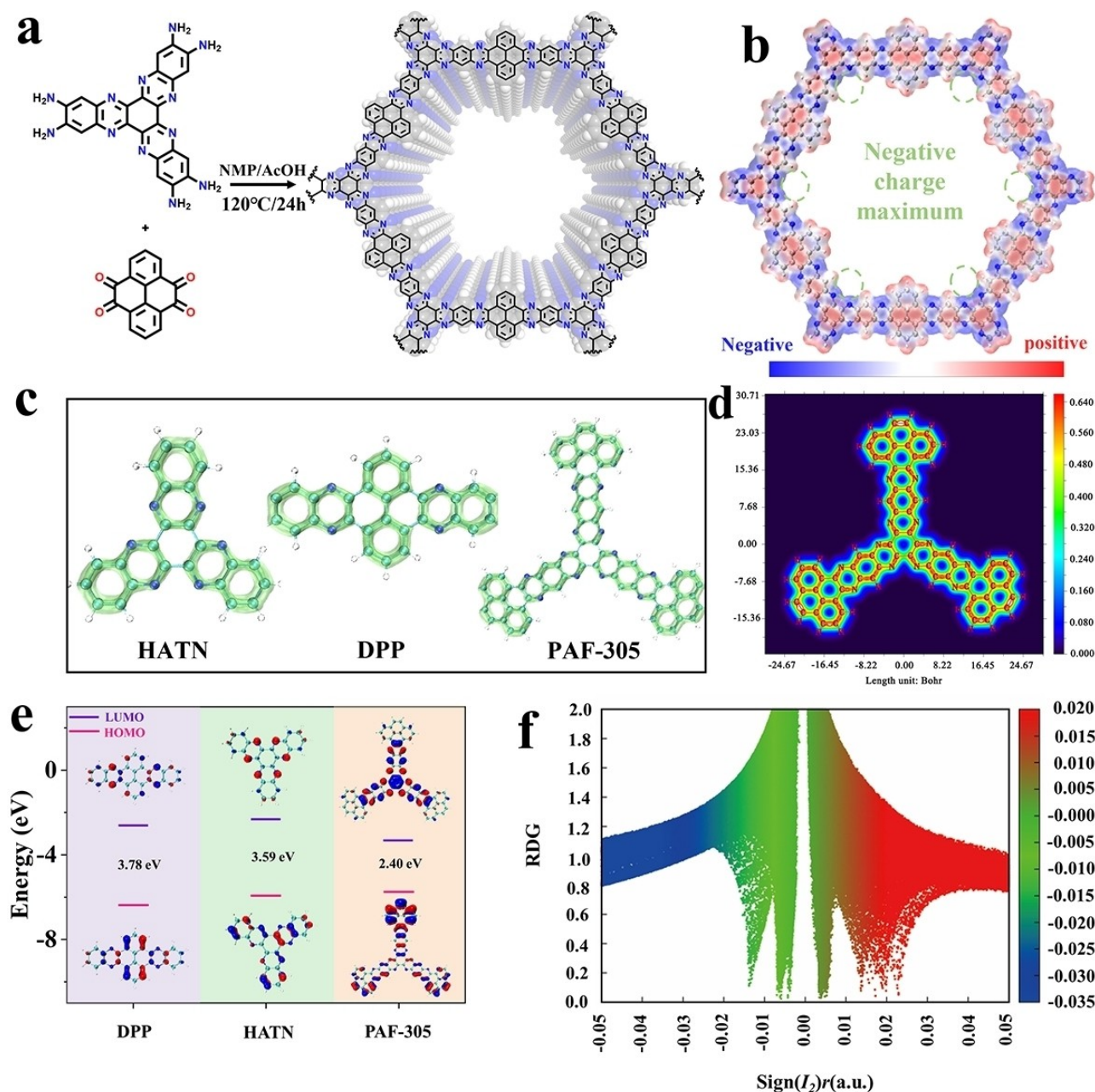


Figure 1. (a) The synthesis and structures of PAF-305. (b) Mapped electrostatic potential (ESP) diagram of the PAF-305 units. (c) LOL- π maps of HATN, DPP, and PAF-305 units. (d) LOL- π color-filled map of PAF-305 units. (e) Comparison in HOMO, LUMO, and gap energy of HATN, DPP, and PAF-305 units. (f). Scatter map of RDG vs. $|I_2|r$.

H₂O were calculated using the DFT to explore the inherent mechanism of the aforementioned selective plating on the crystal surface.^[17] The adsorption energies of K on the Zn(002) and Zn(101) surfaces are −1.62 and −1.76 eV, respectively, which are less than those of Zn and H₂O (Figures 2e, S9b, and S10). This indicates that K is more readily adsorbed on the Zn surface, leading to a homogeneous distribution of electric fields and a subsequent uniform Zn²⁺ deposition process. Dendrite formation is typically heavily influenced by the distributed ions and electric fields at the anode/electrolyte interface. To confirm the effect of the KOTF addition, finite element

simulations using COMSOL Multiphysics were also performed.^[18] In the Zn(OTF)₂ electrolyte, the electric field distribution around the protrusions on the Zn foil surface is uneven and enhanced. Therefore, as the deposition time increases, the electric field density at the protrusion gradually increases, causing more Zn²⁺ to be preferentially deposited at the tip owing to tip effects, causing the protruding dendrites to gradually grow larger and eventually pierce the diaphragm to form a battery short circuit (Figure 2f). In contrast, the addition of KOTF reduces the electric field density at the protrusions of the Zn significantly. After 800 s, the space

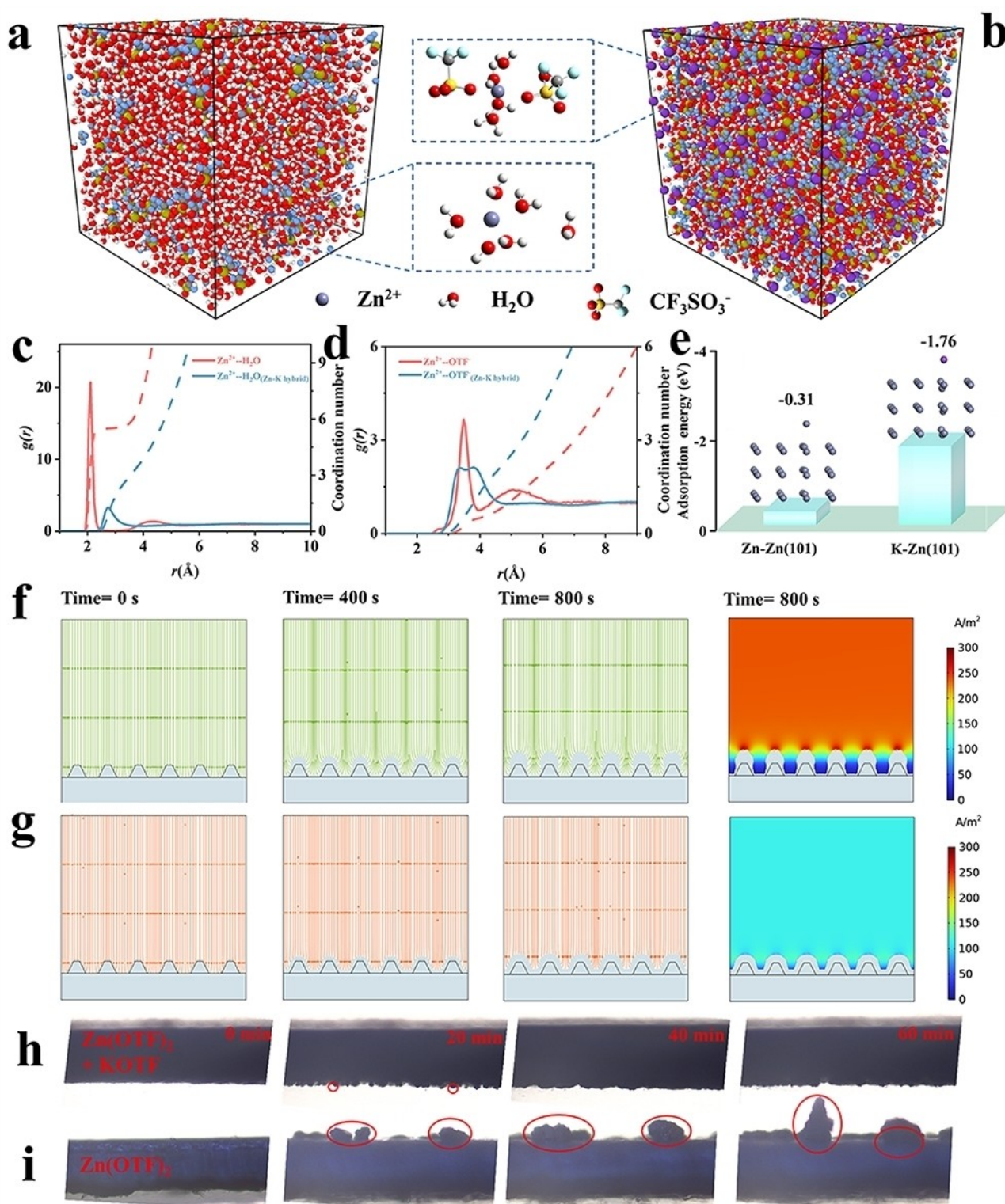


Figure 2. 3D snapshots of (a) Zn(OTF)₂ and (b) Zn-K hybrid ion electrolyte from MD simulations (snapshots of partially enlarged Zn²⁺ solvated structures). RDFs of (c) Zn²⁺-H₂O and (d) Zn²⁺-OTF⁻ for different electrolyte systems. (e) Adsorption energy comparison of Zn and K on Zn(101) crystal planes. Electric field distribution and corresponding Zn²⁺ concentration field distribution on bare Zn with (f) Zn(OTF)₂ and (g) Zn-K electrolyte. Zn deposition morphology on Zn foil in (h) Zn-K and (i) Zn(OTF)₂ electrolytes visualized by in situ optical microscopy.

between the protrusions gradually fills in, resulting in more uniform Zn²⁺ deposition (Figure 2g). Therefore, the introduc-

tion of KOTF can result in a uniform electric field distribution, suppress the tip effect, and form a homogeneous deposition

process without dendrite morphology. The obtained results were then verified using in situ optical microscopy. Dendrites form on the Zn foil surface in the $\text{Zn}(\text{OTF})_2$ electrolyte following 20 min of deposition at 10 mA cm^{-2} . Owing to the tip effect, Zn^{2+} was gradually deposited at the tips of the dendrites, causing them to grow larger and deteriorating the reversibility of the cycle. In contrast, the addition of KOTF resulted in a homogeneous and stable Zn deposition without dendritic growth or gas emission (Figures 2h–i). SEM images of Zn foils after cycles confirmed the inhibitory effect of KOTF on Zn dendrites (Figure S11).

In addition to inhibiting the formation of the tip effect, the introduction of KOTF could increase the number of charge carriers. Compared to K/K^+ , Zn/Zn^{2+} exhibits a higher thermodynamic redox potential, allowing Zn^{2+} to plate or strip preferentially on the anode side, whereas the cathode side binds with K^+ owing to the higher valence state of Zn^{2+} and

significantly slower diffusion rate.^[19] Therefore, these AZKHBs demonstrate a unique work mechanism in which K^+ ions are inserted/extracted at the battery cathode, and Zn^{2+} ions are plated/stripped at the anode (Figure 3a). Furthermore, DFT calculations confirm the preferential interaction reaction of K^+ carriers with the cathode material (Figure 3b and Table S1). Furthermore, electrochemical properties of the PAF-305 was investigated using three electrolytes. The GCD curves with $\text{Zn}(\text{OTF})_2$ exhibit a transition discharge phenomenon when the voltage is less than 0.2 V (Figure S12). Compared to the KOTF, the GCD and the CV curves with Zn–K electrolyte exhibit similar redox peaks (Figure S13a), indicating similar storage mechanisms. In contrast, the battery with Zn–K electrolyte exhibits impressive rate performance (particularly at higher current densities) and improved cycling stability (capacity retention of 98.5 vs. 57.8 %) following 200 cycles when compared to the KOTF electrolyte (Figures 3c

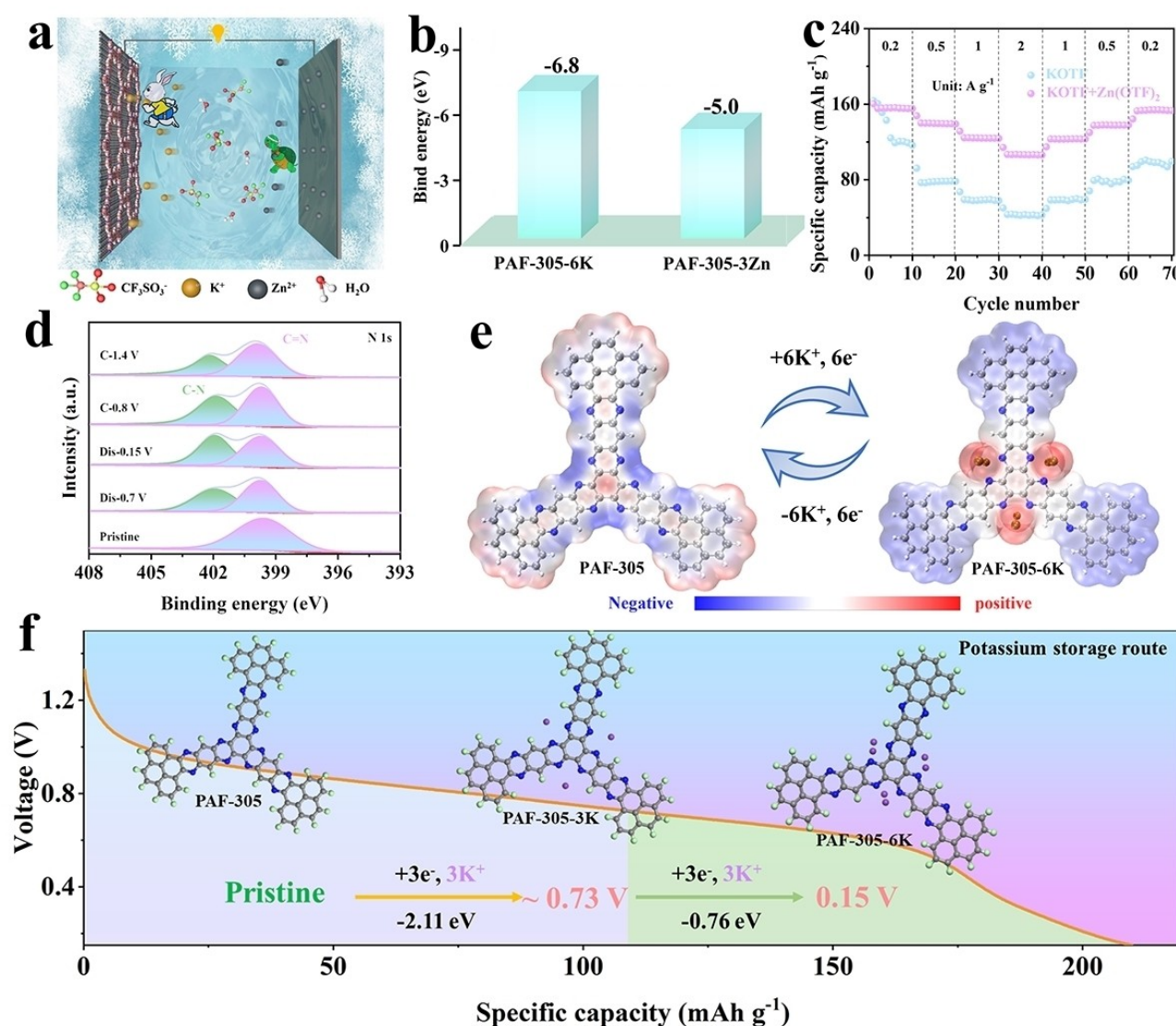


Figure 3. (a) The diagram of the working mechanism for AZKHBs. (b) Binding energies of the PAF-305 unit with different metals by DFT calculation. (c) Rate capability of PAF-305 with KOTF and Zn–K electrolytes. (d) XPS spectra of N 1s of PAF-305 during the GCD processes. (e) Mapped electrostatic potential (ESP) diagram of the PAF-305 unit and PAF-305-6K. (f) Calculated potential storage route of K^+ .

and S13b). To identify the storage mechanism of PAF-305, ex situ XPS and FT-IR were used in the GCD process. The peaks at 1560 and 1273 cm^{-1} correspond to C=N and C-N bonds, respectively, exhibiting opposite trends during GCD processes (Figure S14a). Furthermore, in the N1s XPS spectra of PAF-305, the signal intensity of the C=N bond decreases and then increases during the GCD process, confirming that the C=N of the HATN is the redox active center of PAF-305 (Figure S3d). Furthermore, the K 2p peaks gradually increase and decrease during the complete discharge/charge processes, respectively,^[20] indicating that the redox reaction of the C=N bond is the reason for K^+ storage (Figure S14b). Furthermore, the structural evolution of the PAF-305 unit was developed by DFT calculations. During the discharge process, the abundant C=N redox sites of the PAF-305 unit can bind K^+ in two steps at binding energies of -2.11 and -0.76 eV, respectively, which is reflected by the ESPs (Figure 3e,f). Furthermore, the binding energy of the PAF-305 unit for binding 9 K^+ is calculated to be -0.89 eV (less than -0.76 eV) indicating that the PAF-305 unit can only store 6 K^+ (Figure S15), which is in agreement with the results of the experiments.

Subsequently, the electrochemical properties of PAF-305 as an AZKHB cathode was thoroughly investigated, using Zn anode and Zn-K as the electrolyte. Organic electrode

materials are known to possess lower conductive properties, affecting rate performance (Figure S16). The typical cyclic voltammetry (CV) curves were measured at $0.15\text{--}1.4$ V and 0.1 mVs^{-1} . The redox peaks at $0.89/0.79$ and $0.80/0.66$ were caused by the reversible binding of C=N to K^+ in the HATN unit of PAF-305 (Figure 4a). The following CV curves nearly overlap, demonstrating the exceptional electrochemical stabilities of PAF-305 as an AZKHBs cathode. Moreover, the galvanostatic charge/discharge curves (Figure S17) exhibit an initial discharge specific capacity (594.6 mAh g^{-1}) owing to air presence in the electrolyte at 0.05 Ag^{-1} . Therefore, the discharge specific capacity of the second cycle is 209.9 mAh g^{-1} , which corresponds to a $6e^-$ transfer. In addition, PAF-305 demonstrates a high reversible capacity (184.3 mAh g^{-1}) after 50 cycles and impressive capacity retention (87.8%) (Figure 4b). Even at 1 and 10 Ag^{-1} , PAF-305 exhibits specific capacities of 113.4 and 64.6 mAh g^{-1} and capacity retention ratios of 84% and 81.5% after 1400 and 1600 cycles, respectively (Figures 4d and S18). As illustrated in Figure 4c, PAF-305 exhibits impressive rate capacities of 174.8 , 160.9 , 143.8 , 127.9 , and 109.6 mAh g^{-1} at 0.1 , 0.2 , 0.5 , 1 , and 2 Ag^{-1} , respectively. Moreover, once the current density is recovered to 0.05 Ag^{-1} , the capacity of AZKHBs is 183.2 mAh g^{-1} , demonstrating remarkable electrochemical reversibility. Fur-

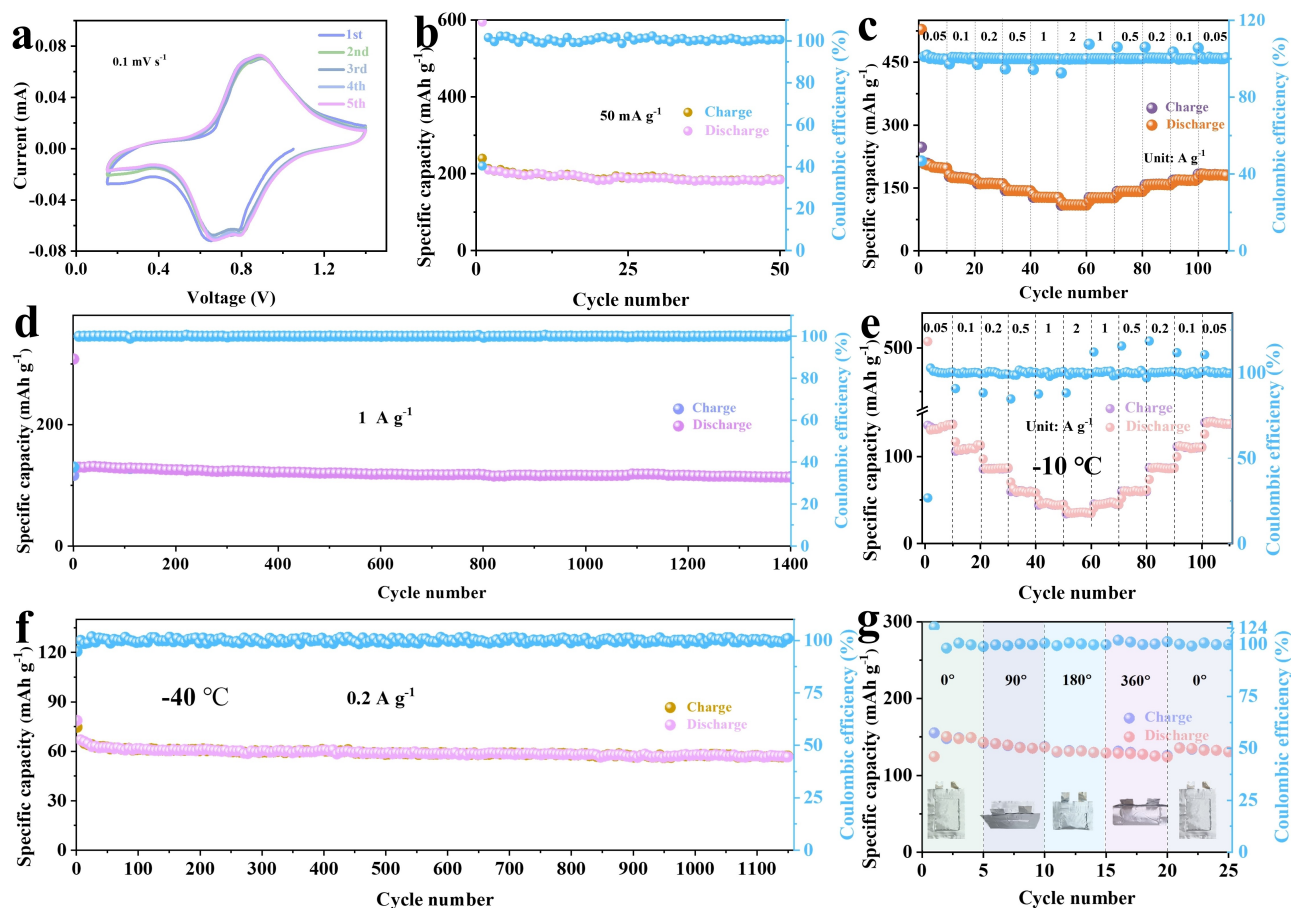


Figure 4. (a) CV curves of PAF-305 at 0.1 mVs^{-1} . (b) Cycling performance of PAF-305 at 0.05 Ag^{-1} . (c) Rate performance of PAF-305. (d) Cycle performance of PAF-305 at 1 Ag^{-1} . (e) Rate performance of PAF-305 under $-10\text{ }^{\circ}\text{C}$. (f) Cycling performance of PAF-305 at $-40\text{ }^{\circ}\text{C}$ at 0.2 Ag^{-1} . (g) The cycling performance of the soft-packaged AZKHBs under different bending states at 0.05 Ag^{-1} .

thermore, electrode reaction kinetics were investigated. The charge transfer resistance (R_{ct}) of PAF-305 electrode decreases with increasing cycles (Figure S19a). The ionic diffusion coefficient of PAF-305 is evaluated to be 10^{-12} to 10^{-10} cm^2s^{-1} (Figure S19b). Encouraged by the impressive battery properties of PAF-305 at 25 °C, the harsh conditions of low temperature (−10 and −40 °C) and high temperature (40 °C) were investigated. As the temperature drops to −10 °C, the rate capacities are 113.5, 97.1, 83.1, 58.2, 44.1, and 36.6 mAh g^{-1} at 0.05, 0.1, 0.2, 0.5, 1, and 2 A g^{-1} , respectively (Figure 4e). The PAF-305 retains good stability following 500 and 2300 cycles at 0.2 and 1 A g^{-1} with capacity retention ratios of 91.2 and 87.5 %, respectively (Figure S20). Excitingly, when the temperature is reduced to −40 °C, PAF-305 continues to function properly, with a capacity of 90 mAh g^{-1} at 0.05 A g^{-1} , and good cycling stability (capacity retention of 78.7 % after 1150 cycles, at 0.2 A g^{-1}) (Figures 4f and S21). The excellent low-temperature performance may be originated from the high-concentration KOTf electrolyte that features high conductivity and low viscosity.^[21] Under high-temperature working conditions of 40 °C, PAF-305 still exhibits a specific capacity (152.2 mAh g^{-1} at 0.2 A g^{-1}) (Figure S22). Subsequently, a flexible packaging battery was then investigated to demonstrate the feasibility of powering flexible electronic devices (Figure 4g). The bending angles of the flexible packaging battery are tested at 0°, 90°, 180°, and 360° (bending a circle back to the initial position),^[22] with specific capacities of 150.9, 139.2, 132.4, and 128.4 mAh g^{-1} , respectively. As the bending angle decreases from 360° to 0°, the specific capacity is restored to 135.6 mAh g^{-1} , indicating a promising application for flexible devices. Moreover, the versatile device boasts impressive rate

performance at 0.05, 0.1, 0.2, 0.5, and 1 A g^{-1} , are 153.8, 117.1, 90.9, 57.6, and 32.5 mAh g^{-1} , respectively. Even if the current density returns to 0.05 A g^{-1} , the corresponding specific capacity can still reach 140.8 mAh g^{-1} following 90 cycles (Figure S23). Subsequently, the stability of the PAF-305 cathode was investigated using self-discharge/charge measurements. After charging to 1.4 V, the PAF-305 maintains a relatively stable voltage platform for 24 h (Figure S24a). The subsequent discharge capacity is almost identical to the normal discharge capacity, and the same results can be observed during the charging process (Figure S24b). Furthermore, the reaction kinetics of PAF-305 were investigated by recording CV curves between 0.15 and 1.4 mV s^{-1} (Figure S25a). As the scan rate increases, similar redox peaks appear accompanied by a slight polarization phenomenon, demonstrating the impressive rate performance of the PAF-305. Furthermore, the electrochemical behavior of the electrodes was investigated using the *b* values calculated from the peak currents corresponding to the scan rates (Equation 1).^[23] The *b* values of the linearly fitted PAF-305 electrode are 0.87, 0.85, 0.83, and 0.82, respectively (Figure S25b), indicating that the charge storage mechanism primarily exhibits pseudocapacitive characteristics. Moreover, the percentages of pseudocapacitive and diffusive properties are further investigated using Equation 2. At 0.2, 0.4, 0.6, 0.8, 1.0, and 1.2 mV s^{-1} , the percentage of pseudocapacitance attributes is 61.3, 67.6, 72.6, 75.4, 79.9, and 82.5 %, respectively (Figures S25c,d).

Finally, the air self-charging behavior of AZKHBs in an open cell system was investigated (Figure 5a). In general, a redox reaction can be triggered by the potential difference between reactants. To investigate the possibility of sponta-

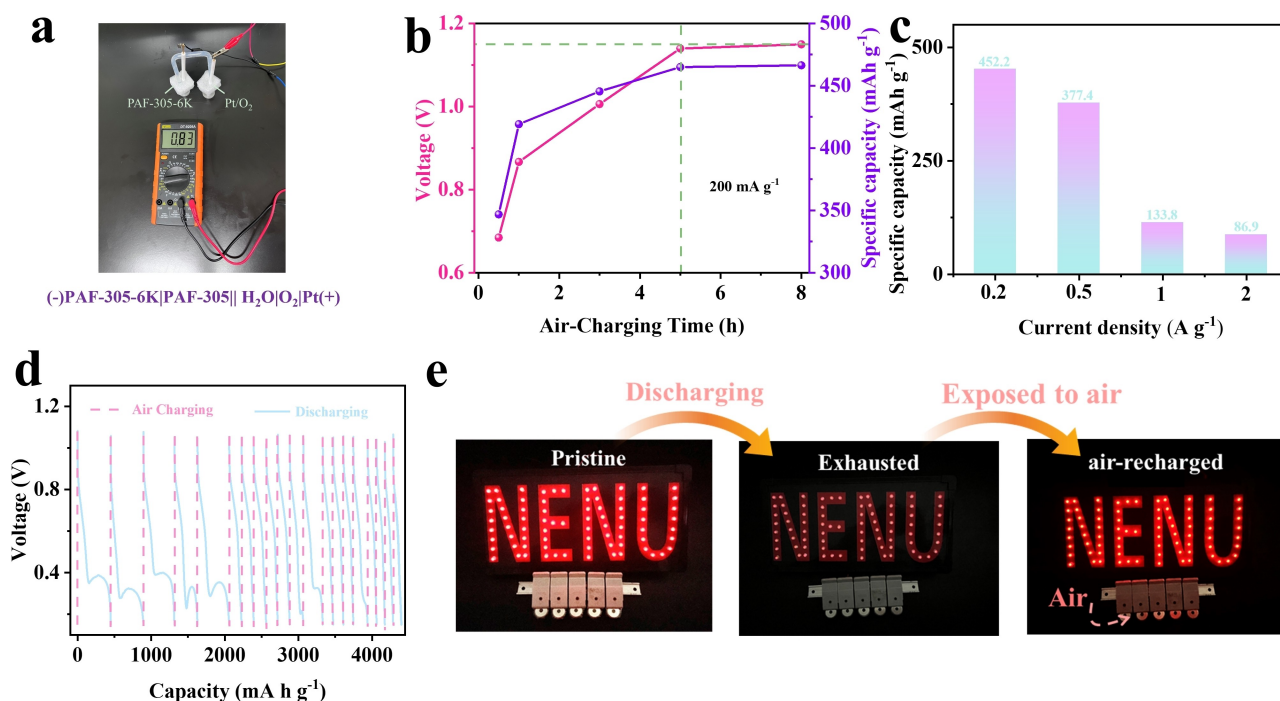


Figure 5. (a) The galvanic cell image of (-)PAF-305-6K|PAF-305||H₂O|O₂|Pt(+). (b) Charge voltage and galvanostatic discharge capacity with different air self-charging times. (c) Discharge capacity at different rates after the air self-charging process. (d) Repeated air self-charging/galvanostatic discharge cycles of AZKHBs. (e) Three different states of the lamp are powered by five air self-charging AZKHBs.

neous reaction, a galvanic cell of $(-)\text{PAF-305-6K}|\text{PAF-305}|\text{H}_2\text{O}|\text{O}_2|\text{Pt}(+)$ was designed, with PAF-305-6K as the anode, the Pt electrode as the cathode, and Zn–K as the electrolyte. The electrolyte at the anode is deoxygenated with N_2 , whereas the cathode is puffed with O_2 . The relationship between the electrochemical thermodynamic function and voltage can be expressed using Equation 3. Encouragingly, the voltage measured across the assembled galvanic cell is 0.83 V, confirming that a redox reaction between PAF-305-6K and O_2 occurs spontaneously. Furthermore, the Gibbs free energy change from DFT calculations expressed by Equation 4 can suggest the spontaneous process. In addition, the assembled galvanic cell produces a higher voltage (0.83 V) than the currently reported air self-charging aqueous batteries (Table S2). Meanwhile, DFT was used to determine whether K^+ charge carriers are more likely to achieve air self-charging properties. The average length of K–N bonds on PAF-305-2 K^+ is 2.65 Å, which is greater than the average length of Zn–N bonds in PAF-305-Zn $^{2+}$ (2.0 Å) (Figure S26). Furthermore, the dipole moment of PAF-305-Zn $^{2+}$ (4.8 a.u.) is smaller than that of PAF-305-2 K^+ (13.0 a.u.), implying that the charge migration from N–K bonds to K^+ is weaker, allowing for an easier self-charging process. When the PAF-305-6K is exposed to air for 4 h, the battery voltage gradually increases and finally stabilizes at 1.13 V. Moreover, the voltage of PAF-305 reaches a maximum of 1.15 V when the battery exposes to air for 8 h. When PAF-305-6K is exposed to pure O_2 flow, the AZKHBs voltage increases sharply at first, then gradually increases to 0.98 V within the first 0.5 h. When the time reaches 2.3 h, the increasing voltage trend slows and tends to 1.13 V. Furthermore, the voltage of PAF-305-6K exposed to N_2 and Ar atmospheres could not be recovered to 1.15 V with increasing time, even after 24 h, which was only owing to the relaxation following the electrical load removal (Figure S27a). Meanwhile, voltage of AZKHBs increases after oxidization, which can also be reflected by galvanostatic discharge capacity. When the PAF-305-6K is exposed to air for 0.5, 1, 3, 5 h, and 8 h (Figures 5b and Figure S27b), AZKHBs exhibit discharge capacities of 346.8, 419.1, 445.4, 464.9 and 466.3 mAhg^{-1} , respectively. Furthermore, the AZKHBs demonstrate the exceptional rate performance. At 0.2, 0.5, 1 and 2 Ag^{-1} , the rate capacities reach 452.2, 377.4, 133.8 and 86.9 mAhg^{-1} , respectively (Figure 5c). As we all know, cycling stability is one of the most important parameters for an air-self-charging battery. The air self-charging AZKHBs assembled with PAF-305 can achieve up to 20 cycles and exhibit a total discharge capacity of up to 4399.6 mAhg^{-1} , enabling an energy density of 2639.8 Whkg^{-1} (Figure 5d). Encouraged by the promising performance of air self-charging AZKHBs at room temperature, harsh conditions including low (-10°C) and ultra-low (-40°C) temperatures were investigated (Figure S28). When the working temperature decreases to -10°C , the air self-charging AZKHBs also demonstrate an accumulated discharge capacity of 1143.5 mAhg^{-1} , allowing for an energy density of 686.1 Whkg^{-1} . As the temperature decreases to -40°C , the air self-charging AZKHBs can still deliver a total discharged

capacity of 518.6 mAhg^{-1} and an energy density of 259.3 Whkg^{-1} . Furthermore, the ex situ FT-IR and XPS also confirmed that the C=N bond acted as a redox center to complete potassium removal process under the oxidation of O_2 (Figure S29). Furthermore, the output voltage of the entire battery device can be adjusted by connecting the batteries in series and parallel to achieve practical scenarios. Two batteries connected in series can generate 2.03 V, which is sufficient to power electronic devices (Figure S30). As a proof-of-concept demonstration of feasibility, five batteries are connected in series to power a large LED device. After batteries are depleted, the devices can be lighted when exposed to air, demonstrating the feasibility of air self-charging AZKHBs (Figure 5e).

Conclusion

In summary, we have successfully constructed a low-temperature chemical self-charging AZKHBs using PAF-305 cathode and redox chemistry with K^+ as charge carriers. Furthermore, the Zn–K electrolyte regulates Zn-ion solvation chemistry to ensure uniform Zn plating/stripping, thereby inhibiting Zn dendrite growth. As expected, the prepared AZKHBs demonstrated exceptional electrochemical performance. Experimental characterization and DFT calculations confirm the abundance of C=N sites in the HATN unit as redox-active centers, revealing a reversible K^+ carrier storage mechanism. Because of the large difference in potentials between the PAF-305-6K cathode material and O_2 in the air, AZKHBs exhibit exceptional chemical self-charging performance. When exposed to air, the voltage of AZKHBs gradually increases to stabilize at 1.14 V after 5 h, and it exhibits an excellent discharge capacity (464.9 mAhg^{-1} at 0.2 Ag^{-1}). Even at -40°C , the AZKHBs exhibit a total discharge capacity of 518.6 mAhg^{-1} and an energy density of 259.3 Whkg^{-1} . Therefore, the integration of an energy harvesting device and battery into the self-charging power system of AZKHBs overcomes the limitation of a lack of a power grid in harsh environments or remote areas, paving the way for future ZIB applications in self-charging systems.

Acknowledgements

This work is financially supported by the National Natural Science Foundation of China (Grant No. 52172186, 22131004, U21A20330), the Science & Technology Department of Jilin Province (No. 20210101116JC), the Fundamental Research Funds for the Central Universities (2412021QD009) and the “111” project (B18012).

Conflict of Interest

The authors declare no conflict of interest.

Data Availability Statement

Research data are not shared.

Keywords: Porous Aromatic Framework • Electron delocalization • Hybrid batteries • Stable Zn anode • Air self-chargeability

- [1] a) X. Jia, C. Liu, Z. G. Neale, J. Yang, G. Cao, *Chem. Rev.* **2020**, *120*, 7795–7866; b) J. F. Parker, C. N. Chervin, I. R. Pala, M. Machler, M. F. Burz, J. W. Long, D. R. Rolison, *Science* **2017**, *356*, 415–418; c) L. S. Cao, D. Li, E. Y. Hu, J. J. Xu, T. Deng, L. Ma, Y. Wang, X.-Q. Yang, C. S. Wang, *J. Am. Chem. Soc.* **2020**, *142*, 21404–1409; d) G. Li, Z. Zhao, S. Zhang, L. Sun, M. Li, J. A. Yuwono, J. Mao, J. Hao, J. Vongsivut, L. Xing, C. Zhao, Z. A. Guo, *Nat. Commun.* **2023**, *14*, 6526; e) G. Zampardi, F. L. Mantia, *Nat. Commun.* **2023**, *13*, 687; f) F. Yue, Z. Tie, Y. Zhang, S. Bi, Y. Wang, Z. Niu, *Angew. Chem. Int. Ed.* **2022**, *61*, e202208513.
- [2] C. Liu, W. Xu, C. Mei, M. Li, W. Chen, S. Hong, W.-Y. Kim, S. Lee, Q. Wu, *Adv. Energy Mater.* **2021**, *11*, 2003902.
- [3] a) Z. Tie, Y. Zhang, J. Zhu, S. Bi, Z. Niu, *J. Am. Chem. Soc.* **2022**, *144*, 10301–10308; b) L. Yan, Y. Zhang, Z. Ni, Y. Zhang, J. Xu, T. Kong, J. Huang, W. Li, J. Ma, Y. Wang, *J. Am. Chem. Soc.* **2021**, *143*, 15369–15377; c) W. Su, Y. Zhang, H. Wang, M. Yang, Z. Niu, *Adv. Mater.* **2023**, *36*, 2308042; d) Y. Zhang, F. Wan, S. Huang, S. Wang, Z. Niu, J. Chen, *Nat. Commun.* **2021**, *11*, 2199.
- [4] a) D. Wang, C. Li, Q. Li, H. Li, J. Rehman, C. Zhi, L. Zhu, *Nano Energy* **2022**, *104*, 107990; b) W. Deng, Z. Li, Y. Ye, Z. Zhou, Y. Li, M. Zhang, X. Yuan, J. Hu, W. Zhao, Z. Huang, C. Li, H. Chen, J. Zheng, R. Li, *Adv. Energy Mater.* **2021**, *11*, 2003639.
- [5] a) L. Zhou, R. Yang, S. Xu, X. Lei, Y. Zheng, J. Wen, F. Zhang, Y. Tang, *Angew. Chem. Int. Ed.* **2023**, *135*, e202307880; b) X. Li, L. Wang, Y. Fu, H. Dang, D. Wang, F. Ran, *Nano Energy* **2023**, *116*, 108858; c) X. Fang, C. Hu, X. Sun, H. Wang, J. Li, *Adv. Energy Mater.* **2023**, *14*, 2302499; d) H. Ren, S. Li, B. Wang, Y. Zhang, T. Wang, Q. Lv, X. Zhang, L. Wang, X. Han, F. Jin, C. Bao, P. Yan, N. Zhang, D. Wang, T. Cheng, H. Liu, S. Dou, *Adv. Mater.* **2023**, *35*, 2208237; e) F. Ming, Y. Zhu, G. Huang, A.-H. Emwas, H. Liang, Y. Cui, H. N. Alshareef, *J. Am. Chem. Soc.* **2022**, *144*, 7160–7170; f) P. Sun, L. Ma, W. Zhou, M. Qiu, Z. Wang, D. Chao, W. Mai, *Angew. Chem. Int. Ed.* **2021**, *60*, 18247–18255.
- [6] G. Liang, Z. Gan, X. Wang, X. Jin, B. Xiong, X. Zhang, S. Chen, Y. Wang, H. He, C. Zhi, *ACS Nano* **2021**, *15*, 17717–17728.
- [7] Z. Tie, Z. Niu, *Angew. Chem. Int. Ed.* **2020**, *59*, 21293–21303.
- [8] a) K. Fan, C. Zhang, Y. Chen, Y. Wu, C. Wang, *Chem* **2021**, *7*, 1224; b) J. Kim, Y. Kim, J. Yoo, G. Kwon, Y. Ko, K. Kang, *Nat. Rev. Mater.* **2023**, *8*, 54–70; c) Y. Lu, Q. Zhang, L. Li, Z. Niu, J. Chen, *Chem* **2018**, *4*, 2786–2813; d) H. Yang, J. Lee, J. Y. Cheong, Y. Wang, G. Duan, H. Hou, S. Jiang, I.-D. Kim, *Energy Environ. Sci.* **2021**, *14*, 4228–4267.
- [9] a) C. Zhang, W. Ma, C. Han, L.-W. Luo, A. Daniyar, S. Xiang, X. Wu, X. Ji, J.-X. Jiang, *Energy Environ. Sci.* **2021**, *14*, 462; b) H. Zhang, L. Zhong, J. Xie, F. Yang, X. Liu, X. Lu, *Adv. Mater.* **2021**, *33*, 2101857; c) Z. Li, J. Tan, X. Zhu, S. Xie, H. Fang, M. Ye, J. Shen, *Energy Storage Mater.* **2022**, *51*, 294–305.
- [10] a) J.-S. M. Lee, A. I. Cooper, *Chem. Rev.* **2020**, *120*, 2171–2214; b) Y. Tian, G. Zhu, *Chem. Rev.* **2020**, *120*, 8934–8986; c) Y. Xu, S. Jin, H. Xu, A. Nagai, D. Jiang, *Chem. Soc. Rev.* **2013**, *42*, 8012.
- [11] a) J. Yu, N. Li, H.-G. Wang, B. Gao, B. Wang, Z. Li, *Chem. Eng. J.* **2023**, *463*, 142434; b) H.-G. Wang, Q. Wu, L. Cheng, G. Zhu, *Coord. Chem. Rev.* **2022**, *472*, 214772; c) Y. Chen, J. Li, Q. Zhu, K. Fan, Y. Cao, G. Zhang, C. Zhang, Y. Gao, J. Zou, T. Zhai, C. Wang, *Angew. Chem. Int. Ed.* **2022**, *134*, e202116289.
- [12] R. Xiao, J. M. Tobin, M. Zha, Y.-L. Hou, J. He, F. Vilela, Z. Xu, *J. Mater. Chem. A* **2017**, *5*, 20180.
- [13] a) Z. Tie, S. Deng, H. Cao, M. Yao, Z. Niu, J. Chen, *Angew. Chem. Int. Ed.* **2022**, *61*, e202115180; b) Z. Song, L. Miao, Y. Lv, L. Gan, M. Liu, *Angew. Chem. Int. Ed.* **2023**, *135*, e202309446.
- [14] T. Sun, Z. Yi, W. Zhang, Q. Nian, H. J. Fan, Z. Tao, *Adv. Funct. Mater.* **2023**, *33*, 2306675.
- [15] W. Li, H. Xu, H. Zhang, F. Wei, L. Huang, S. Ke, J. Fu, C. Jing, J. Cheng, S. Liu, *Nat. Commun.* **2023**, *14*, 5235.
- [16] a) C. Xie, S. Liu, W. Zhang, H. Ji, S. Chu, Q. Zhang, Y. Tang, H. Wang, *Angew. Chem. Int. Ed.* **2023**, *62*, e202304259; b) X. Feng, P. Li, J. Yin, Z. Gan, Y. Gao, M. Li, Y. Cheng, X. Xu, Y. Su, S. Ding, *ACS Energy Lett.* **2023**, *8*, 1192–1200.
- [17] X. Yang, W. Li, Z. Chen, M. Tian, J. Peng, J. Luo, Y. Su, Y. Zou, G. Weng, Y. Shao, S. Dou, J. Sun, *Angew. Chem. Int. Ed.* **2023**, *135*, e202218454.
- [18] a) D. Wang, D. Lv, H. Liu, S. Zhang, C. Wang, C. Wang, J. Yang, Y. Qian, *Angew. Chem. Int. Ed.* **2022**, *134*, e202212839; b) L. Bai, Z. Hu, C. Hu, S. Zhang, Y. Ying, Y. Zhang, L. Li, H. Zhang, N. Li, S. Shi, S. Liu, L. Hao, T. Liu, H. Huang, H. Huang, Y. Zhang, *Angew. Chem. Int. Ed.* **2023**, *62*, e202301631.
- [19] J. Zhan, W. Zhu, Y. Liu, M. Li, J. Zhao, H. Su, J. Ding, J. Sun, Y. Xu, *Adv. Funct. Mater.* **2023**, *33*, 2301935.
- [20] X.-X. Luo, W.-H. Li, H.-J. Liang, H.-X. Zhang, K.-D. Du, X.-T. Wang, X.-F. Liu, J.-P. Zhang, X.-L. Wu, *Angew. Chem. Int. Ed.* **2022**, *134*, e202117661.
- [21] a) L. Jiang, Y. Lu, C. Zhao, L. Liu, J. Zhang, Q. Zhang, X. Shen, J. Zhao, X. Yu, H. Li, X. Huang, L. Chen, Y.-S. Hu, *Nat. Energy* **2019**, *4*, 495–503; b) J. Ge, L. Fan, A. M. Rao, J. Zhou, B. Lu, *Nat. Sustain.* **2022**, *5*, 225–234.
- [22] a) D. Shen, A. M. Rao, J. Zhou, B. Lu, *Angew. Chem. Int. Ed.* **2022**, *61*, e202201972; b) F. Wan, L. Zhang, X. Wang, S. Bi, Z. Niu, J. Chen, *Adv. Funct. Mater.* **2018**, *28*, 1804975.
- [23] Z. Ye, S. Xie, Z. Cao, L. Wang, D. Xu, H. Zhang, J. Matz, P. Dong, H. Fang, J. Shen, M. Ye, *Energy Storage Mater.* **2021**, *37*, 378–386.

Manuscript received: January 22, 2024

Accepted manuscript online: April 15, 2024

Version of record online: May 13, 2024